

A Geometry Map-Based Propagation Model for Urban Channels

Junzhe Song, *Student Member, IEEE*, Ruisi He, *Senior Member, IEEE*, Mi Yang, *Member, IEEE*,
Zhengyu Zhang, *Student Member, IEEE*, Shuaiqi Gao, Bo Ai, *Fellow, IEEE*,

Abstract—With the rapid deployment of 5G and future 6G networks, accurate modeling of urban radio propagation has become critical for system design and network planning. However, conventional statistical or empirical models fail to fully capture the influence of detailed geometric features in dense urban environments. In this paper, we propose a geometry map-based propagation model that directly extracts key parameters from a 3D geometry map and incorporates the Uniform Theory of Diffraction (UTD) to recursively compute multiple diffraction fields, thereby enabling accurate prediction of large-scale path loss and time-varying Doppler characteristics in urban channels. A significant buildings identification algorithm is developed to efficiently detect buildings that significantly affect signal propagation. The proposed model is validated using urban measurement data, showing excellent agreement with path loss in both LOS and NLOS conditions. In particular, for NLOS scenarios with complex diffraction mechanisms, it outperforms the 3GPP and simplified models, reducing the RMSE by 7.1 dB and 3.18 dB, respectively. Doppler analysis further demonstrates its accuracy in capturing time-varying propagation characteristics, confirming the scalability and generalization capability of the model in urban environments.

Index Terms—Map-based channel model, UTD, channel measurements, building identification

I. INTRODUCTION

URban environments have emerged as one of the critical scenarios in the design and deployment of next-generation wireless communication systems. With the advancement of 5G and the evolution towards 6G [1], the demands of applications such as intelligent transportation, vehicle-to-everything (V2X) [2], [3], and smart cities are continuously increasing, making reliable communication in dense urban areas a fundamental requirement [4], [5]. Characterized by tall buildings and narrow streets, urban environments present highly complex propagation environments where signals are severely affected by reflections, diffractions, and blockages [6], [7].

In general, urban channels exhibit the following characteristics [8]: i) *pronounced multipath effects*: Reflectors such as buildings and walls generate a large number of discrete multipath components (MPCs), leading to significantly greater delay spread and angular spread compared to open areas. ii) *strong time variability and non-stationarity*: The movement of the transmitter (TX) and receiver (RX), together with the presence

of dynamic scatterers in the environment, causes the channel characteristics to evolve rapidly over time. iii) *non-uniform angular spreads*: In urban canyon scenarios, the azimuthal spread is usually much larger than the elevation spread, while intersections introduce additional scattering paths. iv) *remarkable environmental dependence*: Channel characteristics are highly dependent on street geometry and building distribution, exhibiting strong site-specific correlations. Therefore, channel models capable of accurately capturing urban environmental features and faithfully reflecting the propagation mechanisms are essential.

Map-based channel models represent an important category of site-specific propagation models that integrate environmental geometry into channel characterization [9]. Unlike stochastic models that rely on statistical fitting, map-based models utilize digital maps or 3D geometric databases to reconstruct the propagation environment, enabling more accurate modeling of path loss, MPCs, and spatial correlation. Representative standardization efforts, such as the 3GPP TR 38.901 hybrid map-based model [10], incorporate map-based extensions to enhance realism in urban and indoor scenarios by combining deterministic ray-tracing with geometry-informed stochastic processes. Similarly, the METIS [11] and WINNER II [12] frameworks adopt map-based modeling to support location-dependent channel generation and mobility-aware simulations. These developments highlight the increasing emphasis on geometry-aware modeling as wireless communication systems evolve toward higher frequencies and denser deployments. Despite these advances, most standardized map-based models still rely on deterministic simulation engines, where environmental information serves only as static input rather than as part of an inference process. Therefore, establishing a propagation model that directly extracts and utilizes environmental parameters from geometric maps and that derives channel characteristics based on physical propagation principles is essential. Such a model would provide a scalable and physically interpretable framework for accurately predicting radio channel behavior across diverse urban canyon environments [13].

Several measurements and models for map-based channels have been carried out [14]–[35]. These models mainly fall into three categories: i) *geometry-based deterministic channel models (GDCMs)*: These models characterize MPC parameters in a fully deterministic manner, typically relying on ray-tracing methods [36]. Their accuracy depends on detailed knowledge of building layouts, street geometries, and material properties [9]. However, the strong reliance on environmental information limits their applicability in large-scale simulations, real-time

J. Song, R. He, M. Yang, Z. Zhang, S. Gao, and B. Ai are with the School of Electronics and Information Engineering, Beijing Jiaotong University, Beijing 100044, China (email: 25115063@bjtu.edu.cn; ruisi.he@bjtu.edu.cn; myang@bjtu.edu.cn; 21111040@bjtu.edu.cn; 25110046@bjtu.edu.cn; boai@bitu.edu.cn).

evaluations, or scenarios with incomplete environmental data [37]. ii) *Hybrid map-based model*: These models combine deterministic methods for dominant paths with statistical models for small-scale scattering [24]–[25], balancing realism and efficiency. However, their parameters require extensive calibration, limiting accuracy and generalization with scarce data, and their adaptability in dynamic environments remains limited. iii) *Data-driven approach*: These models use high-resolution maps or point clouds to train neural networks for predicting path loss, delay–angle spectra, or radio maps, showing strong potential for rapid inference. Physics-informed learning and domain adaptation further reduce the gap between simulated and measured data [26]–[35]. However, their main limitations lie in the reliance on large amounts of labeled data, challenges in generalization, and the high retraining cost when the propagation environment undergoes significant changes.

In addition, several map-based models incorporate the Uniform Theory of Diffraction (UTD) or the Geometrical Theory of Diffraction (GTD) [38]. Within the framework of geometrical optics, UTD/GTD introduce diffraction coefficients and asymptotic field solutions to accurately describe electromagnetic wave diffraction at geometric discontinuities such as building edges and corners, thereby maintaining path continuity even under nonline-of-sight (NLOS) conditions. This characteristic gives UTD/GTD inherent advantages in map-based modeling tasks. For instance, Du et al. derived a Fock-type integral-based “uniform correction term” that enables more physically consistent predictions near shadow boundaries, making UTD more suitable for use in map-based ray-tracing and preventing artificial interference artifacts [39]. Ortiz et al. developed an analytical/semi-analytical model using geometrically mapped urban blocks as input, combining GO and UTD to quantify diffraction and shadowing losses around street corners, and conducted an in-depth analysis of D2D link coverage [40]. Jarndal et al. further examined the diffraction loss approximation strategies adopted by map-based models such as METIS that employ GTD/UTD formulations [41].

However, most of these models still remain constrained by the ray-tracing framework, as their core computational processes rely heavily on path enumeration and recursive ray tracing, leading to a rapid increase in computational complexity with growing scene geometrical detail. Moreover, early studies on UTD/GTD are often conducted under idealized “sandbox” geometries, such as single wedges or limited edge structures, which, while verifying theoretical correctness, maintained a weak connection to real-world map environments and do not fully exploit the potential of map data in environmental modeling [42]–[45]. More importantly, these models typically consider only single-edge diffraction, failing to effectively capture multiple diffraction phenomena occurring among several building edges. Consequently, in complex urban block configurations, discrepancies remain in predicting signal attenuation and path continuity within shadowed regions. Therefore, the application of UTD/GTD theories in large-scale map-based channel modeling continues to face challenges related to high algorithmic complexity, strong dependence on geometric details, and insufficient characterization of multiple diffraction

effects.

In this paper, we propose a geometry map-based propagation model that extracts key geometric parameters from a 3D urban map and incorporates UTD to recursively compute multiple diffraction fields, enabling the derivation of essential channel characteristics such as path loss, multipath delay, and Doppler distributions. The main contributions are summarized as follows:

- We propose the geometry map-based propagation model, by loading the geometry map and setting the transceiver position, the model can automatically reason out the propagation law and loss of channel.
- We set the boundary conditions for propagation more accurately based on UTD and derive a recursive equation for multiple diffraction of the signal between buildings.
- We propose a significant buildings identification algorithm that automatically detects, within the geometric map, buildings that significantly affect the signal propagation path.
- We conduct urban channel measurements and model validation, demonstrating that the proposed model achieves excellent agreement with measured results under both LOS and NLOS conditions, and accurately reproduces Doppler characteristics, confirming its physical accuracy and generalization capability.

The remainder of this paper is organized as follows: Section II outlines the proposed propagation model. Section III presents the significant buildings identification. Section IV details the measurement and validation. Section V concludes the paper.

II. SYSTEM MODEL

In this section, we propose a geometry map-based propagation model to characterize electromagnetic wave behavior in urban environments. The model extracts key geometric parameters from geometry maps. Based on the UTD, the model derives recursive formulations of multiple-diffraction electric fields and computes the corresponding path loss and doppler characteristics at the RX.

A. Environmental geometric Parameterization

In the proposed geometry map-based propagation model, the geometric parameters describing the urban environment are obtained directly from the geometry map database, enabling accurate characterization of each propagation segment determined by the geometry of TX, buildings, and RX, as illustrated in Fig. 1. The input parameters of the model are defined as follows:

- **1) Distance vector between the TX and the buildings.** This parameter is used to calculate the free space loss, which is the primary factor in signal attenuation. This can be expressed as:

$$d = \{d_{l,1}, d_{l,2}, \dots, d_{l,m}, d_{r,1}, d_{r,2}, \dots, d_{r,n}\} \quad (1)$$

- **2) Distance vector between adjacent buildings.** This parameter describes the propagation distance between

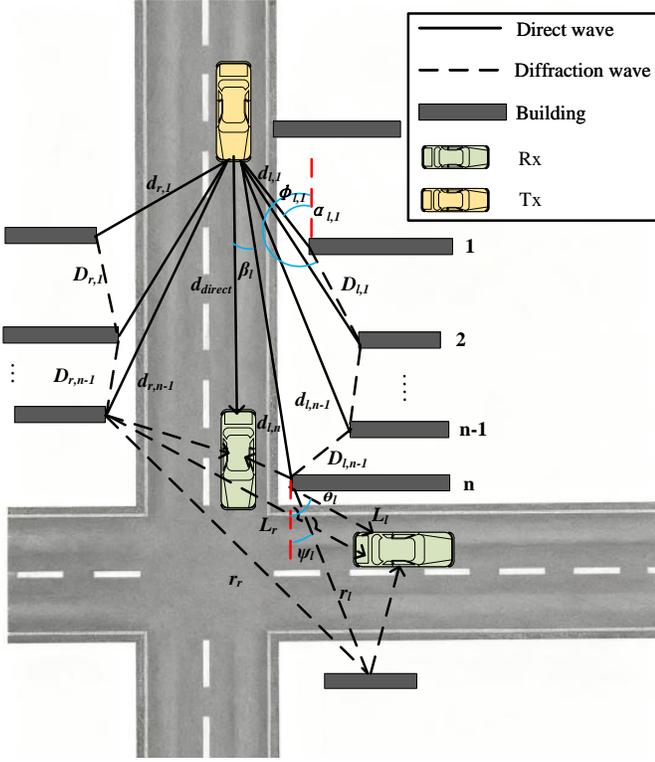


Fig. 1. Diagram of signal propagation in an urban environment.

successive segments in the process of multiple diffractions. This can be expressed as:

$$D = \{D_{l,1}, D_{l,2}, \dots, D_{l,m}, D_{r,1}, D_{r,2}, \dots, D_{r,n}\} \quad (2)$$

- **3) Incident angle and wedge angle.** The incident angle α_i and wedge angle ϕ_i are defined as the angles between the incident wave direction and the normal of the wedge surface. They are used to determine the propagation region and to calculate the diffraction coefficients. These two angles dictate whether the signal is in the reflection, transmission, or diffraction region, thereby controlling the transition between different propagation mechanisms.

B. Boundary Conditions

In urban electromagnetic propagation environments, building edges, corners, and surfaces cause electromagnetic waves to exhibit markedly different propagation characteristics in distinct regions, as illustrated in Fig. 2. According to the UTD [38], the propagation path at a wedge boundary can be divided into three physical regions. We assume $0 \leq \alpha \leq 90^\circ$ and distinguish three wedge regions defined by the half-plane and the directions corresponding to the reflected and transmitted rays:

$$\begin{aligned} \text{reflection region (AOB):} & \quad 0 \leq \phi \leq \alpha \\ \text{transmission region (BOC):} & \quad \alpha \leq \phi \leq 2\pi - \alpha \\ \text{shadow region (COA):} & \quad 2\pi - \alpha \leq \phi \leq 2\pi \end{aligned}$$

In the case where $90^\circ \leq \alpha \leq 180^\circ$, the angle α is redefined such that it still lies within the range $0 \leq \alpha \leq 90^\circ$. The three wedge regions are now:

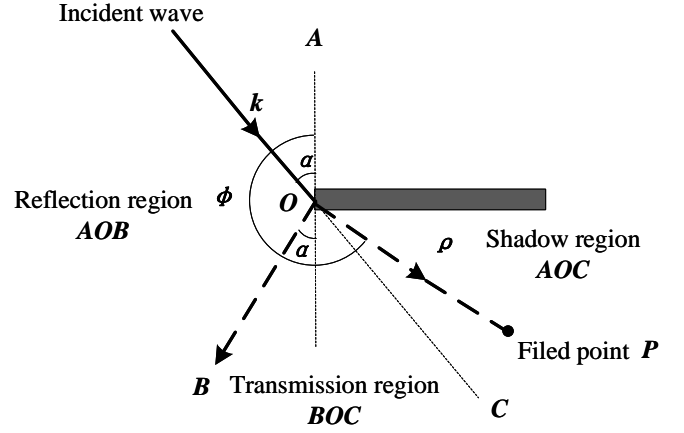


Fig. 2. Propagation behavior of signals on building surfaces.

$$\begin{aligned} \text{reflection region (AOB):} & \quad 0 \leq \phi \leq \pi - \alpha \\ \text{transmission region (BOC):} & \quad \pi - \alpha \leq \phi \leq \pi + \alpha \\ \text{shadow region (COA):} & \quad \pi + \alpha \leq \phi \leq 2\pi \end{aligned}$$

According to [38], the following electromagnetic fields exist within the three regions:

$$\begin{aligned} \text{reflection region:} & \quad E_z = E_t + E_r + E_d \\ \text{transmission region:} & \quad E_z = E_t + E_d \\ \text{shadow region:} & \quad E_z = E_d \end{aligned}$$

We defined the incident, reflected, and diffracted fields:

$$\begin{aligned} E_t &= E_0 e^{jkD \cos \phi_i} \\ E_r &= -E_0 e^{jkD \cos \phi_r} \\ E_d &= -E_0 e^{-jkD} \frac{1-j}{2\pi^2 \sqrt{\frac{k}{\pi D^{\frac{1}{2}}}}} \left(\frac{1}{\cos\left(\frac{\phi_i}{2}\right)} - \frac{1}{\cos\left(\frac{\phi_r}{2}\right)} \right) \end{aligned} \quad (3)$$

where $k = \frac{2\pi}{\lambda}$ is the wavenumber determined by the carrier wavelength λ , and E_0 is the incident electric field strength, and now:

$$\begin{aligned} \phi_i &= \phi - \alpha \\ \phi_r &= \phi + \alpha \end{aligned} \quad (4)$$

C. Multiple diffraction and recursive field calculations

In a multi-diffraction propagation chain, the transmission of the electric field can be regarded as a stepwise recursive process. Suppose the signal sequentially passes through n scattering points, such as building corners or edges; then the electric field received at the i -th scattering point consists of two components: (1) the composite field E_z from the previous propagation stage and (2) the free-space attenuation component along the current propagation path, calculated based on geometric positions. The electric field can be expressed as:

$$E_{dir} = \frac{2\sqrt{15P_t}}{d} e^{-jkd} \quad (5)$$

where P_t denotes the transmitted power of the signal source. To characterize multi-stage propagation effects, the electric field at each stage must be computed recursively, so that the

field at any stage depends not only on the distance of the current propagation path, but also on the phase and amplitude resulting from the diffraction of previous stage. As shown in Fig. 1, the total electric fields at the first and second buildings can be expressed as follows:

$$\begin{aligned} E_1 &= E_{dir}(d_1) \\ E_2 &= E_{dir}(d_2) + E_z[E_1, \phi_1, \alpha_1, D_1] \end{aligned} \quad (6)$$

The total electric field at level i can be expressed recursively as follows:

$$E_n = E_{dir}(d_n) + E_z[E_{n-1}, \phi_{n-1}, \alpha_{n-1}, D_{n-1}] \quad (7)$$

In the implementation, the initial condition for recursive propagation is the direct field E_1 at the first scattering point, after which E_2, E_3, \dots, E_n are successively calculated through the transfer function at each stage. The key advantage of recursive computation is that it allows the electric field to be propagated layer-by-layer along multiple diffraction paths without explicitly evaluating the full propagation integral for each path. Moreover, each stage of propagation in the model directly corresponds to physically observable quantities, such as propagation distance, incident and outgoing angles, and building distribution, thereby providing clear physical interpretability.

D. Total field calculation at the RX

For the final stage of propagation, the electric field is influenced not only by the cumulative effects of multi-stage diffraction but also by the spatial propagation from the breakpoint to the RX. This process forms the final electric field E_{final} , representing the field component generated by diffraction from the last scattering point to the RX, which constitutes the terminal field distribution of the entire propagation chain.

Based on the presence or absence of direct visibility between the TX and RX, propagation can be categorized into LOS and NLOS scenarios. In LOS scenarios, the RX simultaneously receives both the direct field from the TX and the diffracted field originating from the breakpoint. In NLOS scenarios, the direct path is blocked, so the RX can only capture the composite field resulting from multiple diffractions and reflections. Consequently, the total field in NLOS conditions includes additional reflection components and phase superposition effects. The two cases are discussed separately below.

In LOS scenarios, there exists a directly visible propagation path between the TX and RX. In addition to the direct free space field, diffracted components generated by building edges are also present. When the signal propagates from the TX through several diffraction points and undergoes a final diffraction at the breakpoint before reaching the RX, it forms the final electric field component E_{final} . Therefore, the total electric field at the RX in an LOS scenario can be expressed as:

$$\begin{aligned} E_{LOS} &= E_{dir} + E_{final}^{(1)} \\ E_{final}^{(1)} &= E_n D_s^{(I)} A_I e^{-jkL} \end{aligned} \quad (8)$$

where $E_{final}^{(1)}$ denotes the end winding field component after multiple windings [46].

Unlike LOS scenarios, the total electric field in NLOS conditions involves additional propagation mechanisms. After undergoing diffraction at the breakpoint, the signal also experiences reflections from buildings within the NLOS region. Consequently, the final electric field includes not only the first diffracted path but also composite components from reflected paths. The total electric field in an NLOS scenario can be expressed as:

$$E_{NLOS} = E_{final} + E_{dir} \quad (9)$$

$$E_{final} = E_n D_s^{(I)} A_I e^{-jkL} + R_{H,V} E_n D_s^{(II)} A_{II} e^{-jkr}$$

where the first term of E_{final} corresponds to the field component of the bypassed path, and the second term is the complex field reflected by the surface and then bypassed.

Where A^I, A^{II} are amplitude coefficients, affected by the physical parameters from the breakpoint to the RX, indicating the influence of the path geometry, which can be expressed as:

$$\begin{aligned} A^I &= \sqrt{\frac{d_n}{L(d_n + L)}} \\ A^{II} &= \sqrt{\frac{d_n}{r(d_n + r)}} \end{aligned} \quad (10)$$

Let ε_r be the relative permittivity of the reflecting building wall. Thus, R_H and R_V can be calculated as

$$R_{H,V} = \frac{\cos\theta - a_{H,V} \sqrt{\varepsilon_r - \sin^2\theta}}{\cos\theta + a_{H,V} \sqrt{\varepsilon_r - \sin^2\theta}} \quad (11)$$

where $a_H = 1$ and $a_V = 1/\varepsilon_r$ correspond to R_H and R_V , respectively. As $\varepsilon_r \rightarrow \infty$, implying a perfectly conducting wall, one obtains $R_H = -1$ and $R_V = 1$. Results published in the literature on mobile radio communications indicate that the value of ε_r makes negligible differences to the propagation measurements and calculations [46].

$D_s^{(I)}, D_s^{(II)}$ are the diffraction coefficients corresponding to the two paths, respectively, calculated based on the modified Fresnel integral:

$$\begin{aligned} D_s^{(II)} &= \frac{-e^{-j\pi/4}}{2\sqrt{2\pi k}} \\ &\left(\frac{F(X_1)}{-\sin((\theta - \beta)/2)} - \frac{F(X_2)}{-\cos((\theta + \beta)/2)} \right) \end{aligned} \quad (12)$$

Moreover, X_1 and X_2 are defined by

$$\begin{aligned} \sqrt{X_1} &= \sqrt{2kL^{II}} |\sin[(\theta - \beta)/2]| \\ \sqrt{X_2} &= \sqrt{2kL^{II}} |\cos[(\theta + \beta)/2]| \\ L^{II} &= \frac{r}{1 + r/d_n}. \end{aligned} \quad (13)$$

The expression of $D_s^{(I)}$ follows the same form as $D_s^{(II)}$, with the substitution of $\theta \rightarrow \psi$ and $L^{II} \rightarrow L^I = \frac{L}{1 + L/d_n}$.

Furthermore, $F(X)$ is the transition function defined in [46]. In the actual computation, it is appropriate to write for $F(X) \approx \sqrt{\pi X} e^{j(\pi/4 + X)}$. In other cases, it is advantageous to write as follows:

$$\begin{aligned} F(X) &= \sqrt{\pi X} e^{j(\pi/4 + X)} \\ &- 2j\sqrt{X} e^{jX} \int_0^{\sqrt{X}} e^{-j\tau^2} d\tau \end{aligned} \quad (14)$$



Fig. 3. 3D geometric map.

E. Path Loss Calculation

After multiple diffractions and recursive field superposition, the resulting electric field strength must be converted into received power to compute the path loss. The received power is determined by the square of the electric field strength and its relationship with the intrinsic impedance of free space. According to the fundamental principles of electromagnetics, the power density per unit area can be expressed as:

$$S = \frac{|E_i|^2}{2\eta_0}, \quad i \in \{\text{LOS}, \text{NLOS}\} \quad (15)$$

where $\eta_0 = 120\pi$ is the intrinsic impedance of the free space. Under far-field conditions, the effective aperture of the receiving antenna is related to wavelength λ and antenna gain G_r as follows:

$$A_e = \frac{G_r \lambda^2}{4\pi} \quad (16)$$

Thus, the received power can be expressed as:

$$P_r = \frac{\lambda^2 G_r |E_i|^2}{8\pi\eta_0} \quad (17)$$

Finally, the total path loss can be expressed as:

$$PL_{dB} = -10 \log_{10} \left(\frac{P_r}{P_t} \right) \quad (18)$$

Through the above computational procedure, the model establishes a mapping from environmental geometry parameters to path loss. By inputting geometry parameters, the model recursively computes the electric field strength at the RX and ultimately determines the path loss. For different building layouts and street widths, variations in propagation distance and wedge angle among input parameters lead to differences in diffraction coefficients. By dynamically updating these input quantities, the model enables continuous prediction of path loss in complex urban environments.

F. Doppler Characteristics

In time-varying wireless channels, the Doppler effect serves as a key feature characterizing the dynamic behavior of the channel. It can be obtained by simulating the RX motion

TABLE I
NOTATION FOR SIGNIFICANT BUILDINGS IDENTIFICATION

Symbol	Definition
TX	Transmitter position
RX, r	Receiver position (candidate point along route)
bp	Breakpoint (intersection point for NLOS case)
\mathcal{B}	Set of all buildings in the map
\mathcal{B}_{side}	Candidate buildings located on each side of TX–RX (Algorithm 1 output)
\mathcal{B}_{vis}	Final set of visible buildings after filtering
V	Vertex set of buildings
$f_{block}(\cdot)$	Occlusion test function: check if line segment is blocked by building faces
$f_{proj}(\cdot)$	Projection function: compute orthogonal projection of a point onto a line
$f_{side}(\cdot)$	Side classification function: determine whether a point lies on the left/right side of a line
LOS flag	Boolean indicator whether TX–RX is LOS
\mathcal{B}_{left}	Buildings on the left side of bp–RX (NLOS case only)

along a road trajectory. Specifically, at each sampling position, the model calculates the angle of arrival and the path power of all propagation paths reaching the RX, from which the corresponding Doppler shifts are derived. The collection of these Doppler shifts over spatial positions, together with their statistical measure—the RMS Doppler spread—provides a quantitative description of the Doppler characteristics.

For a single propagation path, the Doppler shift is determined by the projection of the RX velocity onto the direction of wave propagation, expressed as:

$$f_{d,i} = \frac{v \cdot \hat{u}_i}{\lambda} \quad (19)$$

where v is the RX velocity vector and \hat{u}_i denotes the unit vector of the incident path direction. At a given RX position, the model aggregates the Doppler shifts of all effective paths $\{f_{d,1}, f_{d,2}, \dots, f_{d,M}\}$, using the received path power P_i as a weighting factor to compute the power-weighted RMS Doppler spread, which can be expressed as:

$$\sigma_d = \sqrt{\frac{\sum_i P_i (f_{d,i} - \bar{f}_{d,w})^2}{\sum_i P_i}}, \quad \bar{f}_{d,w} = \frac{\sum_i P_i f_{d,i}}{\sum_i P_i} \quad (20)$$

This formulation captures the distinct contributions of different propagation paths to the overall Doppler spectrum. By coupling geometric features from map data with the previously derived recursive electric field computation model, the framework enables the generation of spatially continuous Doppler field distributions across the environment.

III. SIGNIFICANT BUILDINGS IDENTIFICATION

The 3D geometric map serves as the source of physical parameters for the model input, as shown in Fig. 3. Based on this map information, we propose a significant buildings identification algorithm designed to automatically detect buildings that have a significant impact on the signal propagation path. The algorithm consists of two core modules: initial building identification and visible building identification. The former determines the set of buildings located on both sides of the propagation path that may potentially act as scatterers, while

Algorithm 1 Initial Building Identification

Require: TX, RX route, V , F , G

Ensure: \mathcal{B}_{side} : candidate buildings classified by side

- 1: Initialize $\mathcal{B}_{side} \leftarrow \emptyset$
- 2: **for** each RX position r in RX route **do**
- 3: Compute vector $\vec{d} \leftarrow r - TX$
- 4: Determine LOS/NLOS:
- 5: **if** $\neg \bigcup_{f \in F} f_{block}(TX, r, f)$ **then**
- 6: LOS \leftarrow True
- 7: **else**
- 8: LOS \leftarrow False
- 9: **end if**
- 10: **if** LOS **then**
- 11: **for** each building group $g \in G$ **do**
- 12: Select vertices $p \in V_g$ within TX–RX segment
- 13: $p_{proj} \leftarrow f_{proj}(p, TX - r)$
- 14: Retain top-level vertices
- 15: **for** each vertex p **do**
- 16: $side(p) \leftarrow f_{side}(p, TX - r)$
- 17: **end for**
- 18: Add g to \mathcal{B}_{side} according to vertex sides
- 19: **end for**
- 20: **else**
- 21: Compute breakpoint bp along RX direction
- 22: Repeat LOS procedure for TX–bp vector
- 23: For bp–RX vector, consider only left-side buildings
- 24: Append results to \mathcal{B}_{side}
- 25: **end if**
- 26: **end for**
- 27: **return** \mathcal{B}_{side}

the latter refines this set by applying occlusion detection and projection-based geometric analysis to eliminate obstructed buildings, thereby obtaining the final set of significant buildings.

A. Map and Parameter Setting

The 3D geometric map is composed of a set of vertex V , a set of faces F , and a set of building groups G . Each building consists of multiple polygonal surfaces, with vertex coordinates stored in either geographic or local coordinate systems. The positions of the TX and RX are defined by measurement trajectories or simulation paths, and the system analyzes the propagation geometry point by point along the RX movement trajectory.

For clarity of the algorithmic description, Table I lists the main symbols and their corresponding meanings used in the building identification process. In practical computation, the system first determines the straight-line direction between the TX and RX as the reference propagation vector, based on which it identifies potential buildings located within the propagation corridor. When occlusion occurs, the algorithm automatically calculates the breakpoint (bp) along the NLOS path and performs identification and filtering separately within the two subsegments, TX–bp and bp–RX. This ensures the feasibility of the model and physical consistency under NLOS

Algorithm 2 Visible Building Identification

Require: \mathcal{B}_{side} , V , TX, r , LOS flag for current RX, bp if NLOS

Ensure: \mathcal{B}_{vis} : set of visible buildings

- 1: Initialize $\mathcal{B}_{vis} \leftarrow \emptyset$
- 2: **if** LOS **then**
- 3: $\mathcal{B}_{check} \leftarrow \mathcal{B}_{side}$
- 4: **else**
- 5: $\mathcal{B}_{check} \leftarrow \mathcal{B}_{side}$ along TX–bp
- 6: $\mathcal{B}_{left} \leftarrow$ left-side buildings along bp–RX
- 7: Append \mathcal{B}_{left} to \mathcal{B}_{check}
- 8: **end if**
- 9: **for** each side in {left, right} **do**
- 10: Sort $\mathcal{B}_{check}[side]$ by perpendicular distance to relevant line
- 11: occlusionFlag \leftarrow False
- 12: **for** each building B in sorted order **do**
- 13: isVisible \leftarrow True
- 14: **for** each vertex $v \in B$ **do**
- 15: $v_{proj} \leftarrow f_{proj}(v, \text{relevant line})$
- 16: **for** each previously accepted building B' in \mathcal{B}_{vis} **do**
- 17: **if** $f_{block}(v, v_{proj}, V_{B'})$ **then**
- 18: isVisible \leftarrow False
- 19: occlusionFlag \leftarrow True
- 20: **break**
- 21: **end if**
- 22: **end for**
- 23: **if** not isVisible **then break**
- 24: **end if**
- 25: **end for**
- 26: **if** isVisible **then**
- 27: Add B to \mathcal{B}_{vis}
- 28: **end if**
- 29: **end for**
- 30: **end for**
- 31: **return** \mathcal{B}_{vis}

conditions. The detailed mathematical definitions of the auxiliary functions used in the identification process are provided in the Appendix.

B. Initial Building Identification

The initial building identification algorithm aims to select candidate scatterers from the global building set that potentially affect the propagation path. The core idea is to identify buildings located near the TX–RX propagation path through geometric projection and occlusion analysis and to classify them according to their position on either side of the path, providing input for subsequent visibility determination.

The algorithm inputs include the TX, RX trajectory, V , F , and G . The output is the set of classified candidate building \mathcal{B}_{side} , divided into left and right groups. The main steps are as follows:

First, for each position point r along the RX trajectory, the vector $\mathbf{d} = r - TX$ is calculated to determine the propagation

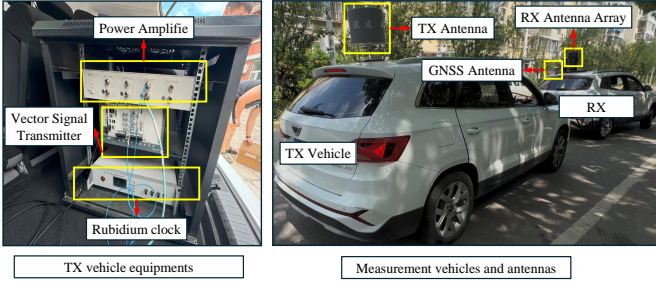


Fig. 4. Measurement system architecture and key equipment.

direction from the transmitter to the receiver. Next, occlusion detection is performed along this propagation line to determine whether any building face $F_f \in F$ blocks the line of sight between TX and r . If no occlusion exists, the location is defined as a LOS scenario; otherwise, it is identified as a NLOS scenario.

In the LOS case, the algorithm traverses all building groups $G_g \in G$ and selects those whose vertex sets are located near the TX–RX line segment. Then, through the projection function $f_{\text{proj}}(\cdot)$, the projection coordinates of each vertex along the propagation direction are calculated to exclude low-level or rear-side vertices outside the effective propagation range, retaining only the top or boundary vertices. For retained vertices, the function $f_{\text{side}}(\cdot)$ is invoked to determine their lateral position relative to the propagation direction, thus completing the left–right-hand classification of scatterers. Finally, the buildings are assigned to the set $\mathcal{B}_{\text{side}}$ according to their side classification.

In NLOS scenarios, the algorithm first computes the breakpoint bp , defined as the intersection point between the TX–RX direction and the obstructing building, which divides the TX–RX line into two propagation segments: TX– bp and bp –RX. The TX– bp segment repeats the building filtering process used in the LOS case to identify edge buildings responsible for initial diffraction, while the bp –RX segment considers only buildings on the left side, which may contribute to secondary scattering after diffraction. The results from the two segments are then combined to form the complete set of candidates $\mathcal{B}_{\text{side}}$.

C. Visible Building Identification

After obtaining the set of candidate buildings $\mathcal{B}_{\text{side}}$, it is still necessary to determine which buildings actually participate in signal propagation. Based on this, the visible building identification algorithm introduces occlusion detection and geometric projection analysis to construct a visibility filtering process, thereby deriving the final set of visible buildings \mathcal{B}_{vis} .

The algorithm takes as input the candidate building set $\mathcal{B}_{\text{side}}$, the vertex set V , the transmitter TX , the receiver position r , the LOS indicator, and the breakpoint bp for the NLOS conditions. The output is the visible building set \mathcal{B}_{vis} corresponding to the current receiver position. The main steps are as follows:

First, the algorithm determines the buildings to be examined according to the LOS or NLOS condition. In the LOS scenario,

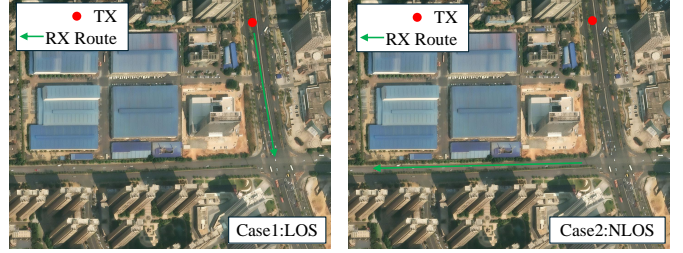


Fig. 5. Measurement Scenarios.

the checking set $\mathcal{B}_{\text{check}}$ is equal to $\mathcal{B}_{\text{side}}$. In the NLOS case, $\mathcal{B}_{\text{check}}$ is composed of candidate buildings along the TX– bp path and the buildings located on the left side of the bp –RX path. This step ensures that all potential propagation paths are covered even under obstructed conditions.

The algorithm then processes the building sets on both sides of the propagation path independently. For each side, the buildings are sorted according to their perpendicular distance to the propagation baseline, and those closer to the baseline are given higher priority for visibility evaluation. For each building B , the projection of each vertex is computed as

$$v_{\text{proj}} = f_{\text{proj}}(v, \text{line}),$$

and occlusion detection is performed sequentially with the surfaces of buildings already identified as visible in \mathcal{B}_{vis} . If the line segment connecting a vertex to its projection is blocked by the set of surfaces $V_{B'}$ of any building $B' \in \mathcal{B}_{\text{vis}}$, the building B is determined to be occluded and excluded from propagation. Otherwise, it is marked as visible and added to \mathcal{B}_{vis} .

The core of the algorithm lies in its hierarchical visibility filtering mechanism. By performing detection and cumulative occlusion assessment in a near-to-far sequence, the algorithm progressively constructs a layered visibility structure, effectively avoiding redundant calculations and unnecessary geometric traversals. Moreover, since the algorithm operates independently at each position RX , it can continuously compute visible scatterer variations along dynamic receiver trajectories, enabling real-time updates of the propagation environment with respect to receiver movement.

The resulting set of \mathcal{B}_{vis} constitutes the effective scatterer ensemble in the current propagation geometry. This set not only reflects the geometric distribution characteristics of urban buildings, but also identifies the key structural elements that influence the propagation of the electromagnetic wave. By integrating this with the physical propagation model proposed in the previous section, the system can visualize real-time changes in building visibility and their effects on path loss, thereby achieving a complete link from geometric modeling to propagation prediction.

IV. VALIDATION AND EVALUATION

We validate and evaluate the proposed propagation model using measured channel data. Comparative analyzes are conducted on two test routes in typical urban canyon environments: one representing LOS conditions and the other NLOS

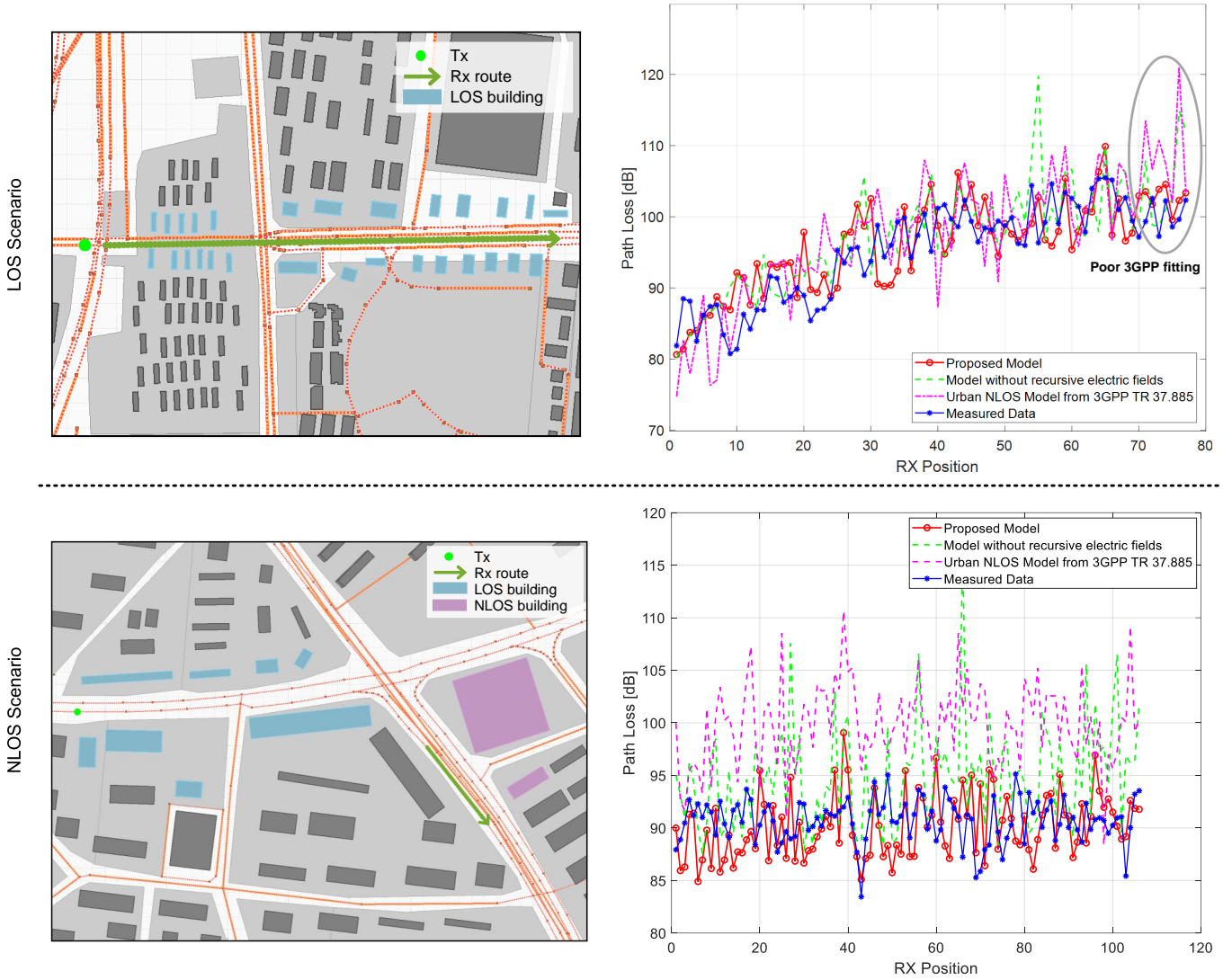


Fig. 6. Path loss comparison between the proposed model, other models, and measured data.

conditions, to assess the applicability of model and prediction accuracy under different propagation scenarios.

A. Measurement Campaign

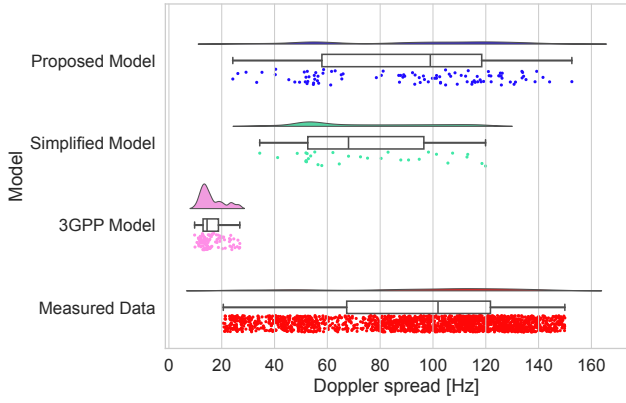
We conducted measurement campaigns using the equipment shown in Fig. 4. The measurement system consists of the TX and RX subsystems integrated into vehicles, with the core components being a vector signal generator (VSG) and a vector signal analyzer (VSA). Specifically, the VSG and VSA are NI PXIe-5673 and NI PXIe-5663, respectively. The sounding signal is a broadband multi-carrier signal with 513 subcarriers over a bandwidth of 30 MHz, centered at 5.8 GHz.

For precise time synchronization, two rubidium clocks disciplined by Global Navigation Satellite System (GNSS) signals are employed. These clocks also provide real-time longitude and latitude coordinates, enabling accurate positioning of both the TX and RX. The measurement bandwidth is 30 MHz, which results in a delay resolution of 33.3 ns. This delay resolution means that only MPCs with propagation distance

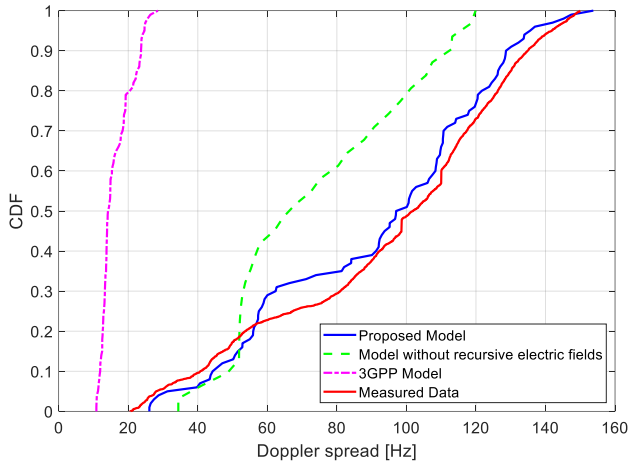
differences exceeding 10 m can be distinguished in the delay domain. For vehicular communications with sub-6 GHz, the available bandwidth is generally 20–30 MHz, which is similar to the measurement configuration in this article. The acquisition rate of channel snapshots is 120 snapshots/s when measured.

The measurements were conducted in Changsha, China. The measurement area covers major roads within a 4 km × 3 km urban district in Fig. 3. The streets under measurement are flanked by densely packed buildings reaching several tens of meters in height, forming a typical urban canyon environment. As illustrated in Fig. 6, the measurement routes comprise two cases:

- **Case1: LOS scenarios.** The TX and RX vehicles were on the same road, with the RX vehicle positioned ahead of the TX vehicle. The TX vehicle was parked at the roadside, while the RX vehicle maintained an average speed of 20 km/h to ensure consistency in data collection.
- **Case2: NLOS scenarios.** The RX vehicle traveled on a



(a)



(b)

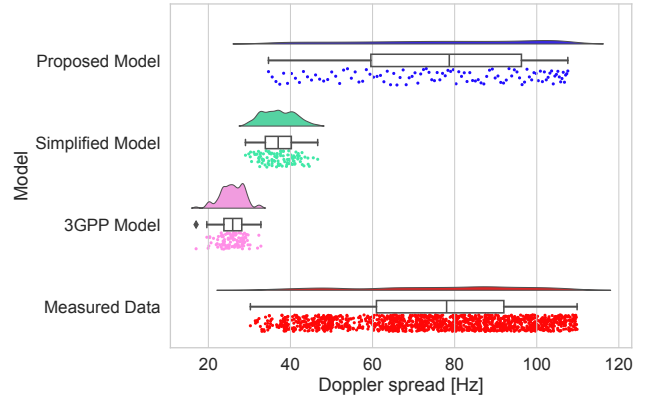
Fig. 7. Doppler Spread Analysis in the LOS Route. (a) Scatter density map. (b) CDF comparison.

road adjacent to and approximately perpendicular to the one where the TX was located. TX vehicles parked on the side of the road at the beginning of the process, and the RX maintained the same speed as in the LOS cases.

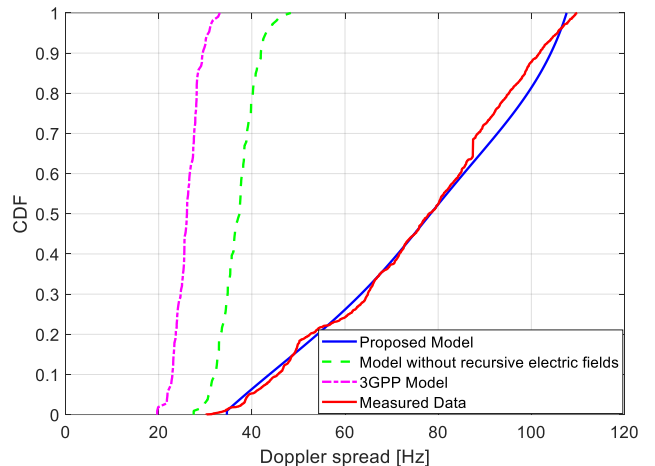
Measurements were conducted in the absence of other nearby vehicles to ensure that additional vehicular movements did not influence the results used for analysis.

B. Path Loss validation

Two test routes are selected from typical urban environments for analysis: one under LOS conditions and the other under NLOS conditions, as shown in Fig. 6. The figure also illustrates the effectiveness of the significant building identification process, where buildings located along both sides of the main propagation path and not blocked by obstacles are accurately detected and highlighted. During model validation, both the measured path loss and the predicted results from three models were calculated for each route: (1) the proposed propagation model, (2) the 3GPP TR 37.885 standard path loss model, and (3) a simplified model that neglects multiple diffraction effects (considering only the propagation from the last diffraction point to the receiver). The root-mean-square error (RMSE) was adopted as the evaluation metric to quantify



(a)



(b)

Fig. 8. Doppler Spread Analysis in the NLOS Route. (a) Scatter density map. (b) CDF comparison.

the deviation between the model predictions and the measured data, as shown in Table II.

In the LOS route, signal propagation is primarily dominated by the direct free-space component. As shown in Fig. 6, all three models capture the overall trend of path loss variation, but noticeable differences appear in local fitting accuracy. The proposed model closely follows the measured results along the entire route, accurately reproducing small-scale fluctuations caused by weak reflections and scattering from surrounding buildings. In contrast, the simplified model and the 3GPP model exhibit evident deviations in certain regions—particularly where local reflections or partial obstructions occur. The simplified model neglects these secondary propagation effects, while the 3GPP model, being purely empirical, fails to account for the geometric characteristics of the actual environment. As a result, both tend to either overestimate or underestimate the path loss in specific segments, leading to reduced local prediction accuracy.

In contrast, the NLOS route presents a much more complex propagation environment. In this case, buildings completely block the line of sight, and the signal relies mainly on diffraction and multiple diffraction effects along building edges. As shown in Fig. 6, the proposed model exhibits

TABLE II
PATH LOSS RMSE COMPARISON

Scenario	Proposed Model (dB)	3GPP TR 37.885 (dB)	Model without recursive electric fields (dB)
LOS	4.65	6.32	5.72
NLOS	3.59	10.69	6.77

a significantly better prediction performance in the NLOS scenario. Specifically, the proposed model achieves an RMSE of 3.59 dB, with the predicted curve closely matching the measured path loss trend, accurately capturing both the abrupt attenuation transitions and local energy enhancement regions. The simplified model yields an RMSE of 6.77 dB, showing larger errors and fluctuations, making it difficult to capture the detailed variations in path loss—further confirming the importance of multiple diffraction mechanisms in urban propagation modeling. The 3GPP standard model exhibits the highest RMSE of 10.69 dB, with generally overestimated results, indicating that traditional empirical models fail to accurately represent the diffraction characteristics caused by building obstructions in NLOS environments.

In general, the proposed propagation model demonstrates stable predictive capability in both LOS and NLOS scenarios, with particularly notable performance improvements in complex urban street-canyon environments. These results confirm that the model effectively captures the combined effects of multiple diffraction, scattering, and reflection mechanisms in urban environments, exhibiting strong generalization ability and practical applicability.

C. Doppler spread validation

Two test routes, as illustrated in Fig. 6, are selected for comparative analysis of Doppler spread characteristics. Each route includes four sets of data: measured results, predictions from the proposed model, results from a simplified model, and estimates from the 3GPP TR 37.885 standard model. The measured Doppler spread is extracted by performing an autocorrelation operation on the channel impulse response (CIR) followed by a Fourier transform. The Doppler spread predicted by the proposed model is obtained using (21), through the calculation of Doppler shifts corresponding to each propagation path. The simplified model neglects multiple diffraction effects and retains only two dominant paths—those formed between the TX and the primary scatterers, namely the buildings located on both sides of the road closest to the receiver. The 3GPP model, based on standardized Urban Macro (UMa) scenario parameters, estimates the Doppler spread statistically using an empirical relationship between the angular spread and the maximum Doppler shift, without relying on specific geometric configurations. Its mathematical formulation can be expressed as:

$$\sigma_d = f_{d,\max} \cdot \sigma_\gamma \quad (21)$$

Here, $\sigma_\gamma = 11^\circ$ denotes the empirical parameter of angular spread, as defined in the 3GPP channel model [10]. To

TABLE III
DOPPLER SPREAD CDF D_{ks} COMPARISON

Scenario	Proposed Model	3GPP TR 37.885	Model without recursive electric fields
LOS	0.09	0.95	0.33
NLOS	0.07	0.99	0.89

comprehensively illustrate the performance of different models in the Doppler domain, all results are comparatively analyzed in two forms: scatter density maps and cumulative distribution functions (CDFs), as shown in Fig. 7 and 8. The former depicts the spatial distribution characteristics of Doppler spread, while the latter reveals the overall statistical behavior and the consistency between model predictions and measurements. In addition, we use the Kolmogorov-Smirnov-test (KS-test) to measure the distance (D_{ks}) between the distributions of the RMS Doppler spread of the synthetic data and measurement data, as shown in Table III. A smaller D_{ks} indicates more similarities between the two distributions.

Overall, the Doppler spread along the LOS route is generally larger than that along the NLOS route. This difference aligns with the physical principles of electromagnetic wave propagation. In LOS scenarios, a dominant direct signal component exists, and the projection angle between the receiver’s motion direction and the incident wave direction varies significantly with position, resulting in a wider distribution of Doppler frequency shifts. In contrast, in NLOS scenarios, the direct path is completely obstructed, and signal propagation primarily relies on diffraction and reflection. Consequently, the received energy tends to be more isotropically distributed, leading to smaller overall Doppler shifts and a narrower spread range. Moreover, in heavily obstructed urban environments, the number of effective propagation paths is limited and the geometric relationships among them remain relatively stable, causing the instantaneous Doppler distribution to become more concentrated.

From the comparison, the proposed model shows good agreement with the measured data under both LOS and NLOS conditions. This consistency arises because the model explicitly accounts for key propagation mechanisms such as geometric constraints imposed by buildings and multiple diffraction effects, thereby accurately capturing the Doppler spread characteristics induced by the combined influence of diffraction, scattering, and reflection. As a result, it provides a more precise representation of the time-varying behavior of the signal. In contrast, the simplified model considers only the direct path and a single dominant scatterer, leading to Doppler spreads that are significantly lower than the measured values. The 3GPP model, which employs a fixed angular spread parameter for empirical estimation, lacks scenario-specific adaptability; consequently, its predicted Doppler spreads remain nearly identical across different conditions and deviate considerably from the experimental results.

V. CONCLUSION

In this paper, we propose a geometry map-based propagation model which directly extracts key geometric parameters

from an urban 3D map database and, by incorporating the UTD, derives a recursive formulation for the calculation of multiple diffraction fields, enabling the derivation of essential channel characteristics such as path loss, multipath delay, and Doppler distributions. In addition, a significant buildings identification algorithm is developed to efficiently filter out building structures that have a significant impact on propagation paths. The model is validated based on measurements. The results show that in typical urban environments, the proposed model accurately characterizes the path loss variations under both LOS and NLOS conditions. Particularly in NLOS scenarios, where propagation mechanisms are more complex, the model achieves markedly higher prediction accuracy than the 3GPP standard model and simplified models neglecting multiple diffraction effects, reducing the RMSE by approximately 7.1 dB and 3.18 dB, respectively. Furthermore, Doppler spread analysis confirms that the model precisely characterizes the time-varying propagation behavior, achieving the closest agreement with measurements among all compared models, thereby validating scalability and generalization ability of the proposed model.

APPENDIX

The following auxiliary functions are introduced to support the geometric identification of buildings relevant to the radio propagation process. Their objective is to determine the visibility relationship between the TX and RX and to characterize the spatial positioning of surrounding scatterers in a three-dimensional environment.

The projection function $f_{\text{proj}}(p, L)$ computes the orthogonal projection of an arbitrary point p onto a given line segment $L = \overline{ab}$, as expressed by

$$f_{\text{proj}}(p, L) = a + \frac{(p - a) \cdot (b - a)}{\|b - a\|^2} (b - a), \quad L = \overline{ab}, \quad (\text{A.1})$$

which provides a geometric reference for assessing the relative position of buildings with respect to the TX–RX line.

The side classification function $f_{\text{side}}(p, L)$ identifies whether a point p lies on the left or right side of the propagation path L , defined as

$$f_{\text{side}}(p, L) = \text{sign}((b - a) \times (p - a))_z, \quad L = \overline{ab}. \quad (\text{A.2})$$

This function enables the algorithm to partition candidate buildings into distinct spatial regions, facilitating side-based visibility filtering.

Finally, the occlusion test function $f_{\text{block}}(a, b, B)$ determines whether the propagation segment \overline{ab} is obstructed by any face of a given building B , formulated as

$$f_{\text{block}}(a, b, B) = \begin{cases} 1, & \exists \text{ face } F \in B \text{ s.t. } \overline{ab} \cap F \neq \emptyset, \\ 0, & \text{otherwise.} \end{cases} \quad (\text{A.3})$$

A value of 1 indicates that building B blocks the direct propagation path, marking the link as NLOS. Together, these functions provide a systematic and physically interpretable framework for identifying relevant buildings and filtering scatterers in urban channel modeling.

REFERENCES

- [1] C. Huang, R. He, B. Ai, A. F. Molisch, B. K. Lau, K. Haneda, B. Liu, C. Wang, M. Yang, C. Oestges *et al.*, “Artificial intelligence enabled radio propagation for communications—part ii: Scenario identification and channel modeling,” *IEEE Transactions on Antennas and Propagation*, vol. 70, no. 6, pp. 3955–3969, 2022.
- [2] R. He, C. Schneider, B. Ai, G. Wang, Z. Zhong, D. A. Dupleich, R. S. Thomae, M. Boban, J. Luo, and Y. Zhang, “Propagation channels of 5G millimeter-wave vehicle-to-vehicle communications: Recent advances and future challenges,” *IEEE vehicular technology magazine*, vol. 15, no. 1, pp. 16–26, 2019.
- [3] Z. Zhang, R. He, B. Ai, M. Yang, X. Zhang, Z. Qi, and Z. Zhong, “Channel semantic characterization for integrated sensing and communication scenarios: From measurements to modeling,” *arXiv preprint arXiv:2503.01383*, 2025.
- [4] V. Vardhan Gudla, V. Babu Kumaravelu, B. Anjana, P. Selvaprabhu, N. Baskar, H. Sheeba John Kennedy, S. Nath Sur, W. Montlouis, A. Lucky Imoize, and A. Murugadass, “Aber performance evaluation of RIS-Aided millimeter wave massive MIMO system under 3GPP 5G channels,” *Massive MIMO for Future Wireless Communication Systems: Technology and Applications*, pp. 347–369, 2025.
- [5] J. Tian, Y. Han, S. Jin, J. Zhang, and J. Wang, “Analytical channel modeling: From MIMO to extra large-scale MIMO,” *Chinese Journal of Electronics*, vol. 34, no. 1, pp. 1–15, 2025.
- [6] R. He, O. Renaudin, V. Kolmonen, K. Haneda, Z. Zhong, B. Ai, and C. Oestges, “Characterization of quasi-stationarity regions for vehicle-to-vehicle radio channels,” *IEEE Transactions on Antennas and Propagation*, vol. 63, no. 5, pp. 2237–2251, 2015.
- [7] Z. Zhang, R. He, M. Yang, X. Zhang, Z. Qi, H. Mi, G. Sun, J. Yang, and B. Ai, “Non-stationarity characteristics in dynamic vehicular isac channels at 28 GHz,” *Chinese Journal of Electronics*, vol. 34, no. 1, pp. 73–81, 2025.
- [8] F. Lyu, H. Zhu, N. Cheng, H. Zhou, W. Xu, M. Li, and X. Shen, “Characterizing urban vehicle-to-vehicle communications for reliable safety applications,” *IEEE Transactions on Intelligent Transportation Systems*, vol. 21, no. 6, pp. 2586–2602, 2019.
- [9] T. Zemen, J. Gomez-Ponce, A. Chandra, M. Walter, E. Aksoy, R. He, D. Matolak, M. Kim, J.-I. Takada, S. Salous, R. Valenzuela, and A. F. Molisch, “Site-specific radio channel representation for 5G and 6G,” *IEEE Communications Magazine*, vol. 63, no. 6, pp. 106–113, 2025.
- [10] Q. Zhu, C. X. Wang, B. Hua, K. Mao, S. Jiang, and M. Yao, “3GPP TR 38.901 channel model,” in *the wiley 5G Ref: the essential 5G reference online*. Wiley Press, 2021, pp. 1–35.
- [11] L. Raschkowski, P. Kyösti, K. Kusume, T. Jämsä, V. Nurmela, A. Karttunen, A. Roivainen, T. Imai, J. Järveläinen, J. Medbo, J. Vihriälä, J. Meinilä, K. Haneda, V. Hovinen, J. Ylitalo, N. Omaki, A. Hekkala, R. Weiler, and M. Peter, “METIS Channel Models (D1.4),” 07 2015.
- [12] P. Kyosti, “WINNER II channel models,” *IST, Tech. Rep. IST-4-027756 WINNER II D1. 1.2 V1. 2*, 2007.
- [13] R. He and B. Ai, *Wireless channel measurement and modeling in mobile communication scenario: Theory and application*. CRC press, 2024.
- [14] P. Kyösti, J. Lehtomäki, J. Medbo, and M. Latva-aho, “Map-based channel model for evaluation of 5G wireless communication systems,” *IEEE Transactions on Antennas and Propagation*, vol. 65, no. 12, pp. 6491–6504, 2017.
- [15] S. Priebe, M. Jacob, and T. Kürner, “Calibrated broadband ray tracing for the simulation of wave propagation in mm and sub-mm wave indoor communication channels,” in *European Wireless 2012; 18th European Wireless Conference 2012*. VDE, 2012, pp. 1–10.
- [16] O. Kanhere and T. S. Rappaport, “Calibration of nyuray, a 3D mmwave and sub-THz ray tracer using indoor, outdoor, and factory channel measurements,” in *ICC 2023-IEEE International Conference on Communications*. IEEE, 2023, pp. 5054–5059.
- [17] M. Gan, G. Steinböck, Z. Xu, T. Pedersen, and T. Zemen, “A hybrid ray and graph model for simulating vehicle-to-vehicle channels in tunnels,” *IEEE Transactions on Vehicular Technology*, vol. 67, no. 9, pp. 7955–7968, 2018.
- [18] J. Pascual-Garcia, J.-M. Molina-Garcia-Pardo, M.-T. Martinez-Ingles, J.-V. Rodriguez, and L. Juan-Llacer, “Wireless channel simulation using geometrical models extracted from point clouds,” in *2018 IEEE International Symposium on Antennas and Propagation & USNC/URSI National Radio Science Meeting*. IEEE, 2018, pp. 83–84.
- [19] I. Carton, W. Fan, P. Kyösti, and G. F. Pedersen, “Validation of 5G METIS map-based channel model at mmwave bands in indoor scenarios,” in *2016 10th European Conference on Antennas and Propagation (EuCAP)*. IEEE, 2016, pp. 1–5.

- [20] Y.-J. Wang, L.-X. Guo, Z.-Y. Liu, and X.-J. Li, "Ray-tracing-based indoor channel prediction using point cloud geometrical modeling," in *2021 13th International Symposium on Antennas, Propagation and EM Theory (ISAPE)*. IEEE, 2021, pp. 1–3.
- [21] M. Ying, D. Shakya, P. Ma, G. Qian, and T. S. Rappaport, "Site-specific location calibration and validation of ray-tracing simulator nyuray at upper mid-band frequencies," *arXiv preprint arXiv:2507.22027*, 2025.
- [22] Y.-G. Lim, Y. J. Cho, M. Sim, Y. Kim, C.-B. Chae, and R. A. Valenzuela, "Map-based millimeter-wave channel models: An overview, hybrid modeling, data, and learning," *arXiv preprint arXiv:1711.09052*, 2017.
- [23] Q. Zhu, H. Li, Y. Fu, C.-X. Wang, Y. Tan, X. Chen, and Q. Wu, "A novel 3D non-stationary wireless MIMO channel simulator and hardware emulator," *IEEE Transactions on Communications*, vol. 66, no. 9, pp. 3865–3878, 2018.
- [24] Q. Zhu, K. Mao, M. Song, X. Chen, B. Hua, W. Zhong, and X. Ye, "Map-based channel modeling and generation for U2V mmwave communication," *IEEE Transactions on Vehicular Technology*, vol. 71, no. 8, pp. 8004–8015, 2022.
- [25] P. Große, C. Schneider, G. Sommerkorn, and R. Thomä, "A hybrid channel model based on winner for vehicle-to-x application," *arXiv preprint arXiv:1601.05929*, 2016.
- [26] A. Alkhateeb, "DeepMIMO: A generic deep learning dataset for millimeter wave and massive mimo applications," *arXiv preprint arXiv:1902.06435*, 2019.
- [27] M. Alrabeiah and A. Alkhateeb, "Deep learning for mmwave beam and blockage prediction using sub-6 GHz channels," *IEEE Transactions on Communications*, vol. 68, no. 9, pp. 5504–5518, 2020.
- [28] A. Alkhateeb, G. Charan, T. Osman, A. Hredzak, J. Morais, U. Demirhan, and N. Srinivas, "DeepSense 6G: A large-scale real-world multi-modal sensing and communication dataset," *IEEE Communications Magazine*, vol. 61, no. 9, pp. 122–128, 2023.
- [29] X. Zhao, Z. An, Q. Pan, and L. Yang, "Nerf2: Neural radio-frequency radiance fields," in *Proceedings of the 29th Annual International Conference on Mobile Computing and Networking*, 2023, pp. 1–15.
- [30] S. Bakirtzis, J. Chen, K. Qiu, J. Zhang, and I. Wassell, "EM DeepRay: An expedient, generalizable, and realistic data-driven indoor propagation model," *IEEE Transactions on Antennas and Propagation*, vol. 70, no. 6, pp. 4140–4154, 2022.
- [31] J. Hoydis, F. Ait Aoudia, S. Cammerer, M. Nimier-David, N. Binder, G. Marcus, and A. Keller, "Sionna RT: Differentiable ray tracing for radio propagation modeling," in *2023 IEEE Globecom Workshops (GC Wkshps)*. IEEE, 2023, pp. 317–321.
- [32] G. Cao and Z. Peng, "Raypronet: A neural point field framework for radio propagation modeling in 3D environments," *IEEE Journal on Multiscale and Multiphysics Computational Techniques*, 2024.
- [33] K. Qiu, S. Bakirtzis, H. Song, J. Zhang, and I. Wassell, "Pseudo ray-tracing: Deep leaning assisted outdoor mm-wave path loss prediction," *IEEE Wireless Communications Letters*, vol. 11, no. 8, pp. 1699–1702, 2022.
- [34] B. Chatelier, L. Le Magoarou, V. Corlay, and M. Criissière, "Model-based learning for location-to-channel mapping," in *ICASSP 2024-2024 IEEE International Conference on Acoustics, Speech and Signal Processing (ICASSP)*. IEEE, 2024, pp. 12 836–12 840.
- [35] S. Fu, Y. Zeng, Z. Wu, D. Wu, S. Jin, C.-X. Wang, and X. Gao, "CKMDiff: A generative diffusion model for CKM construction via inverse problems with learned priors," *arXiv preprint arXiv:2504.17323*, 2025.
- [36] O. Kanhere, H. Poddar, and T. S. Rappaport, "Calibration of NYURay for ray tracing using 28, 73, and 142 GHz channel measurements conducted in indoor, outdoor, and factory scenarios," *IEEE Transactions on Antennas and Propagation*, 2024.
- [37] B. Rainer, M. Hofer, S. Zelenbaba, D. Löschenbrand, T. Zemen, X. Ye, and P. Priller, "Scalable, resource and locality-aware selection of active scatterers in geometry-based stochastic channel models," in *2021 IEEE 32nd Annual International Symposium on Personal, Indoor and Mobile Radio Communications (PIMRC)*. IEEE, 2021, pp. 885–891.
- [38] S. J. Orfanidis, "Electromagnetic waves and antennas," 2002.
- [39] X. Du and J. Takada, "A uniform additional term using fock-type integral to unify edge diffraction creeping diffraction and reflection in lit and shadowed regions," *Prog. Electromagn. Res. B*, vol. 101, no. 6, pp. 101–117, 2023.
- [40] E. Brugarolas-Ortiz, I. Rodríguez-Rodríguez, J.-V. Rodríguez, L. Juan-Llácer, and D. Pardo-Quiles, "Using the uniform theory of diffraction to analyze radio wave propagation along urban street canyons for device-to-device communication," *Electronics*, vol. 12, no. 3, p. 593, 2023.
- [41] A. Jarndal and K. Alnajjar, "MM-wave wideband propagation model for wireless communications in built-up environments," *Physical communication*, vol. 28, pp. 97–107, 2018.
- [42] M. Peter, R. J. Weiler, B. Göktepe, W. Keusgen, and K. Sakaguchi, "Channel measurement and modeling for 5G urban microcellular scenarios," *Sensors*, vol. 16, no. 8, p. 1330, 2016.
- [43] J. Lorente-López, J.-V. Rodríguez, M.-T. Martínez-Inglés, J.-M. M. Garcia-Pardo, I. Rodríguez-Rodríguez, and L. Juan-Llácer, "Analyzing radiowave multiple diffraction from a low transmitter in vegetated urban areas using a spherical-wave UTD-PO approach," *EURASIP Journal on Wireless Communications and Networking*, vol. 2024, no. 1, p. 49, 2024.
- [44] M. Bhatt, "A new solution based on UTD-PO method for multiple-diffraction by a series of buildings with irregular height and spacing," *International Journal of Wireless Information Networks*, vol. 28, no. 2, pp. 217–229, 2021.
- [45] X. Du and J.-i. Takada, "Equivalence of knife-edge diffraction model and uniform geometrical theory of diffraction applying fresnel approximation for an absorbing screen," *Electronics Letters*, vol. 59, no. 22, p. e13014, 2023.
- [46] W. Zhang, "A wide-band propagation model based on UTD for cellular mobile radio communications," *IEEE Transactions on Antennas and Propagation*, vol. 45, no. 11, pp. 1669–1678, 1997.